

Dielectric Elastomer Architectures with Strain-Tunable Permittivity

Maura R. O'Neill, Deanna Sessions, Nitesh Arora, Vincent W. Chen, Abigail Juhl, Gregory H. Huff, Stephan Rudykh, Robert F. Shepherd, and Philip R. Buskohl*

Flexible hybrid electronic (FHE) materials and devices exploit the interaction of mechanical and electromagnetic properties to operate in new form factors and loading environments, which are key for advancing wearable sensors, flexible antennas, and soft robotic skin technologies. Dielectric elastomer (DE) architectures offer a novel substrate material for this application space as they are a class of strain-tolerant and programmable metamaterials that derive their mechanical and dielectric properties from their architecture. Due to their hyperelasticity, dielectric elastomers can leverage reversible finite deformation to physically reconfigure their internal architecture to repeatedly tune their material behavior. Here a combined computational and experimental study of two dielectric elastomer architectures, based on square and hexagonal unit cell periodicities are presented. A shift in effective permittivity is observed due to the relative increase in matrix volume and the rearrangement of the electric field distribution in the cells. Additive fabrication allows rapid unit cell geometry customization for tuning the electromechanical response of the architectures. Effective permittivity shifts $\Delta\epsilon_2 > 0.7$ under compressive strains of 35% are observed. The practical utility of this strain-tunable permittivity is demonstrated in a microstrip patch antenna, which exhibits shifts in resonance frequency greater than 110 MHz when the dielectric elastomer substrate is compressed.

1. Introduction

Metamaterials are functional materials engineered to manipulate their environment as defined by their structure rather


than their intrinsic material constituents. Metamaterials concepts have been demonstrated in diverse fields, including electromagnetics, acoustics, mechanics and others, exhibiting novel properties such as negative refractive index, perfect absorption, and auxetic behavior.^[1–5] Further, metamaterials can be designed with flexible and reconfigurable substrates to achieve physically tunable responses. For instance, several examples of origami and deployable structures exhibit adaptive electromagnetic resonance tuning through physical deformation.^[6–10]

Strain-tunable dielectric materials and composites are a growing research field with recent demonstrations in optical and millimeter wave regimes.^[11,12] For instance, Meerbeek et al., described the macroscopic shape of a porous elastomeric foam by measuring the shift in light reflected internally by its cellular voids during bending and twisting.^[11] Zhang et al., synthesized a graphene foam with tunable microwave absorption via solid matrix densification during physical compression.^[13]

Additional mechanisms for strain-tuning dielectric properties include the use of permanent or induced dipoles at the molecular level; and the distribution of voids and inclusions in host matrices.^[14–16] Elastomeric metamaterials present a deformation-based tuning strategy for regulating local periodicity and effective dielectric properties. This strategy is particularly useful in deformable electromagnetic devices where the feature size of the dielectric architecture is electrically small and physical reconfiguration of the dielectric structure will facilitate localized and controllable tuning.^[14] Materials with mechanically reconfigurable dielectric properties can help address these inherent challenges for flexible hybrid electronics (FHEs) and adaptive communication devices.

Elastomers have previously been leveraged for mechanical metamaterials, which are a subset of metamaterial designs with periodic architectures whose elements rotate, buckle, fold, or snap under an external load.^[17] Mechanical instabilities present in many of these structures allow their rapid transformation under relatively low strains. They demonstrate unique properties like auxetic behavior, energy absorption, multistability, and nonlinear elastic properties.^[18–25] The transformation of these mechanical structures provides a straightforward tuning mechanism for surrounding wave properties in optical, acoustic, and

M. R. O'Neill, R. F. Shepherd
Department of Mechanical and Aerospace Engineering
Cornell University
124 Hoy Road, Ithaca, NY 14850, USA
D. Sessions, G. H. Huff
Department of Electrical Engineering
Penn State University
University Park, PA 16801, USA
N. Arora, S. Rudykh
Department of Mechanical Engineering
University of Wisconsin-Madison
Madison, WI 53706, USA
V. W. Chen, A. Juhl, P. R. Buskohl
Materials and Manufacturing Directorate
Air Force Research Laboratory
Wright-Patterson AFB, OH 45433, USA
E-mail: philip.buskohl.1@us.af.mil

 The ORCID identification number(s) for the author(s) of this article can be found under <https://doi.org/10.1002/admt.202200296>.

DOI: 10.1002/admt.202200296

electromagnetic domains.^[26] Li et al., demonstrated a tunable Poisson's ratio in soft, periodic microstructures with strategically placed stiff inclusions; the placement and orientation of the inclusions also alters the acoustic stop band.^[27,28] Bertoldi et al., introduced an elastomeric architecture consisting of periodic circular holes with auxetic behavior due to the transformation of the holes into alternating, orthogonal ellipses.^[18] Goshkoderia et al., presented a computational study surrounding the tunability of effective permittivity in these dielectric architectures under finite strain.^[29] However, the coupled nature of their mechanical and dielectric properties has yet to be characterized experimentally and demonstrated in a FHE device.

Flexible substrates with tunable permittivity provide a path toward deformable antennas and transmission lines structures that can be engineered for frequency stability or tuning as a response to physical reconfiguration. Current demonstrations of materials in flexible communication devices include textiles and thin polymer films.^[30,31] Thin film substrates offer an alternative for wearable devices, but it becomes difficult to incorporate conductive elements in these devices while maintaining conformability.^[30] Materials currently used in this application space include polydimethylsiloxane (PDMS) and liquid crystal polymers (LCPs), which exhibit low-permittivity for high electromagnetic transmission, are environmentally stable, and are mechanically compliant.^[31–33] Porous elastomer foams are also relevant for FHE applications due to their lightweight and conformable nature; and they maintain flexibility when assembled adjacent to inextensible layers.^[34,35] However, elastomer foams lack structural integrity under cyclic loading.^[35–37] Furthermore, architected elastomers boast programmable properties like mechanical flexibility and effective permittivity; the microstructure of architected elastomers can also be spatially varied for local control of effective properties.^[38,39] The ability to tune these architected elastomers merits the investigation of their utility for FHE applications.

In this study we investigate, both numerically and experimentally, the coupled mechanical and electromagnetic response of two dielectric elastomer (DE) architectures for 3D printed, soft antenna substrates with a tunable frequency response to deformation (Figure 1a). We simulated and experimentally characterized: i) the influence of porosity on the buckling behavior in the architectures and their corresponding effective permittivity shift; ii) the mechanical behavior of the architectures; and iii) the utility of their permittivity shift in controlling the center frequency of a microstrip patch antenna with an architected dielectric substrate. The study provides clear evidence for the dielectric tuning potential of dielectric elastomer metamaterials; it lays the foundation for future optimization of the architecture with increased tuning and device integration.

2. Architecture Design

The dielectric architectures considered in this study consist of two unit cell geometries, square and hexagonal, comprised of low permittivity voids (air, relative permittivity $\epsilon_v = 1$ and void volume fraction c_v) and a high permittivity matrix (elastomeric polyurethane, relative permittivity $\epsilon_m = 4$ and matrix volume fraction c_m ; Figure 1b,c).^[40] During characterization, the bottom

surface of each specimen was fixed to measure the effective permittivity ϵ_2 under an applied electric field E_2 and compressive strain ϵ , both in the $-\hat{e}_2$ direction (ϵ applied to top surface of specimen; Figure 1b,c). The two architectures exhibit distinct buckling patterns that drive a rapid increase in matrix volume fraction. Customizing the porosity of their periodic structures provides a strategy for tuning their response to finite strain—namely, the onset of their mechanical buckling instability and their corresponding shift in effective permittivity. The void diameter, d_v , depends on the void volume fraction, c_v , and the geometric scale of the unit cells. The unit cell width, a , defines the geometric scale for the architectures; the experimental unit cell width for both architectures was $a = 3$ mm. Figure S1, Supporting Information, illustrates the relationship between void diameter and void volume fraction in the experimental specimens. The overall specimen thickness depends on the unit cell height and the number of unit cell rows in the \hat{e}_2 direction; the hexagonal and square architecture specimens had two and three rows of unit cells in the \hat{e}_2 direction, respectively.

Additive manufacturing provides a straightforward method for tuning the porosity of the architectures as well as for customizing their shape and geometric scale, limited only by the printer build size and resolution. We fabricated the samples with digital light processing (DLP), a vat polymerization method, because of its speed (>100 mm h⁻¹) and its printing resolution (100 μ m layer heights; Figure S2, Supporting Information).^[41,42] The matrix material is an elastomeric polyurethane with a sufficiently high permittivity relative to that of air, an important consideration for tuning effective permittivity via deformation ($\epsilon_r = 4$ and 1, respectively).^[40,43] The 3D printed elastomeric polyurethane exhibits high elasticity (tangent modulus $E \approx 5.67$ MPa at $\epsilon = 0.20$ and elongation at break $>350\%$; tensile behavior in Figure S3, Supporting Information) and high dimensional accuracy (± 70 μ m).^[40,43]

In addition to print resolution, their manufacturing quality depends on the removal of uncured liquid pre-polymer from their void channels before their final thermal cure (8 h at 120 °C) with a combination of isopropyl alcohol solvent and compressed air.^[42] As c_v decreases, the diameter of the void channels decreases; if their diameter is too narrow, their size is no longer within the printer capabilities or they become too difficult to clear of uncured liquid resin. Although increasing c_v results in a more flexible substrate, it can also lead to thin, fragile walls between void channels and, ultimately, print failure. Hence, the experimental design parameters of void volume fraction, c_v , and unit cell dimension, a , strike a careful balance between manufacturing feasibility and mechanical stiffness of the composite.

3. Computational Model of Permittivity Tuning Mechanisms

We formulated the coupled electromechanical finite element (FE) simulations to investigate the tunability of effective permittivity in the DE architectures via applied strain. Representative 2D unit cells were evaluated for both square and hexagonal architectures. The mechanical behavior of the soft matrix was defined by a nearly incompressible hyperelastic material with a

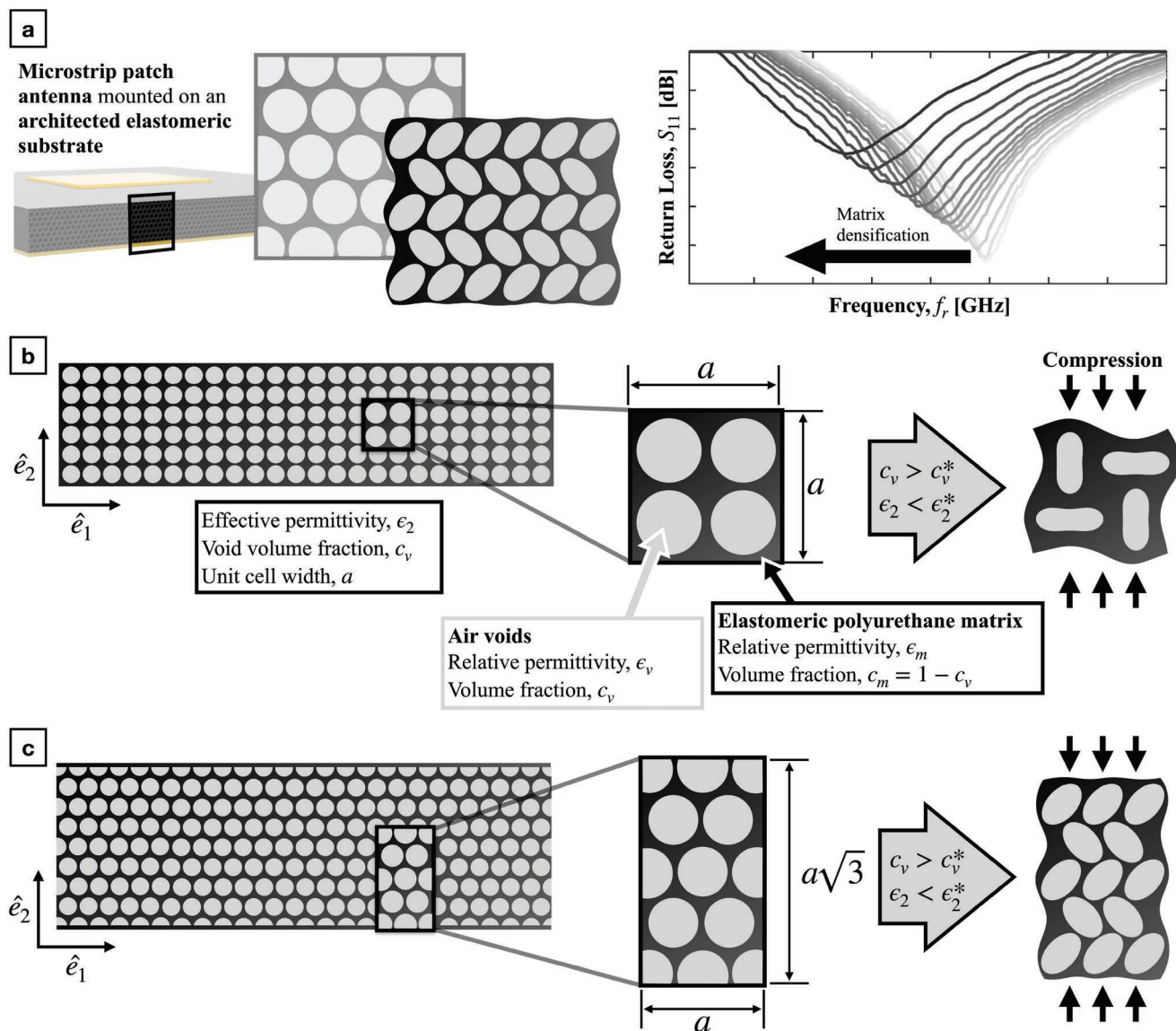


Figure 1. Rendering of architected dielectric antenna substrate and architecture design overview. a) Rendering of architected dielectric elastomer antenna substrate with shifting resonance frequency. b) Undeformed and compressed square unit cells with relevant design parameters (void volume fraction $c_v = 0.65, 0.70$ and unit cell width $a = 3$). c) Undeformed and compressed hexagonal unit cells with relevant design parameters ($c_v = 0.60, 0.70$ and $a = 3$). In both cases, characterization of effective permittivity ϵ_2 conducted with bottom surface of specimens fixed to plane with normal vector \hat{e}_2 . Effective permittivity measured under an applied electric field \mathbf{E}_2 and a compressive strain ϵ applied to the top surface, both in the $-\hat{e}_2$ direction.

neo-Hookean constitutive relation. The architectures were subjected to in-plane compressive strain, ϵ , applied in the \hat{e}_2 direction. An electric field of constant magnitude, E_{app} , was applied along the \hat{e}_2 direction. We applied periodic boundary conditions to the unit cells for the displacement and electric field (see Supporting Information for details).

When compressive loading exceeds a threshold level, the elastomeric architectures develop a mechanical instability; the voids collapse in a cooperative manner leading to internal reconfiguration and an increase in matrix volume fraction (Figure 2a,b; matrix volume fraction during compression in Figure S4, Supporting Information). DE architectures with lower void volume fractions have thicker ligaments and,

therefore, develop instability at higher compressive loading (Figure S5, Supporting Information).^[44] Critical strain values, ϵ_{cr} , corresponding to the onset of instability are indicated by hollow circles in Figure 2c–f. Beyond ϵ_{cr} , the square and hexagonal architectures reconfigure into distinct void shapes. These microstructural transformations directly influence the electric field distribution in the matrix and void subdomains; these transformations are independent of geometric scale (Figure 2a,b).

The effective permittivity of the DE architecture along the applied field is evaluated as $\epsilon_2^* = \bar{D}_2 / (\epsilon_0 \bar{E}_2)$ where E_2 and D_2 are the local electric field and displacement field components, respectively. These are evaluated across unit cell domain Ω

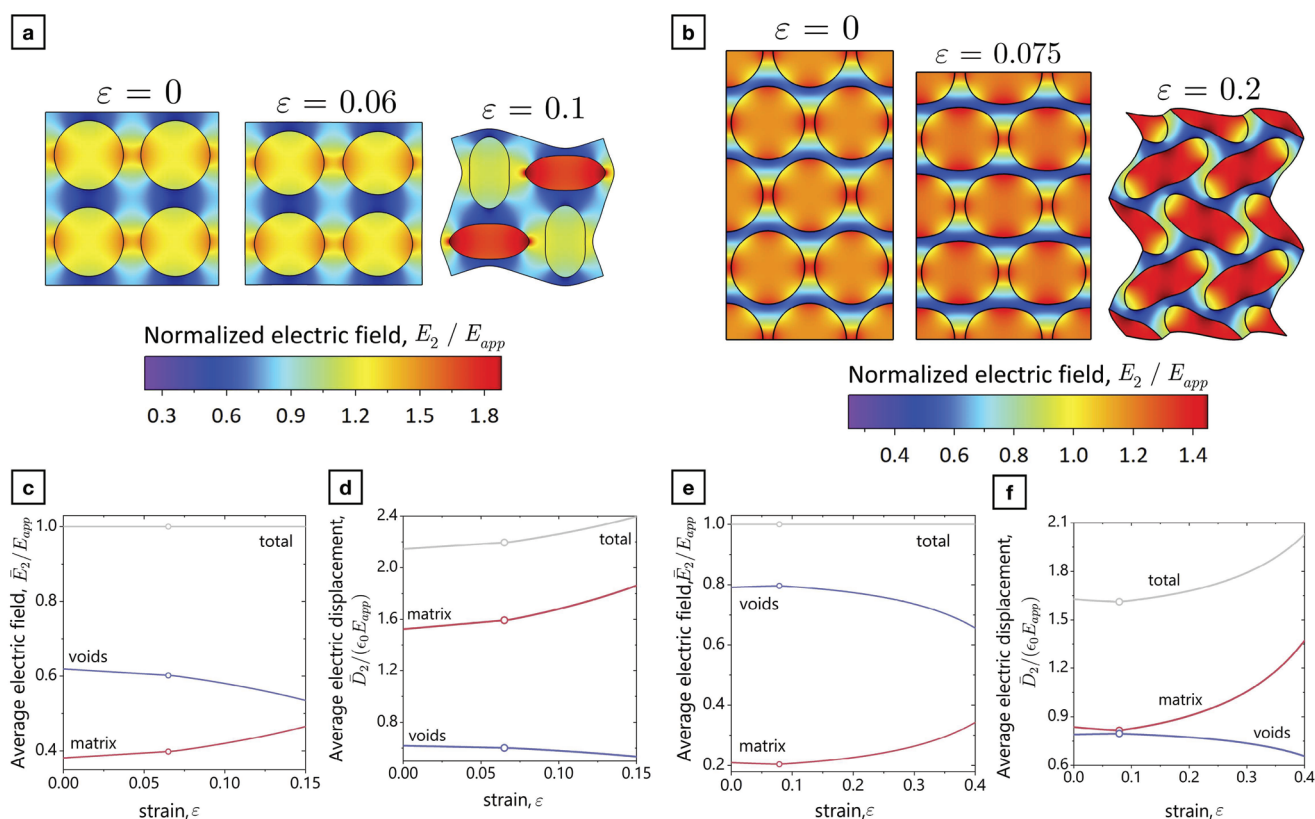


Figure 2. Normalized electric field E_2/E_{app} distribution in a) square, $c_v = 0.50$, and b) hexagonal, $c_v = 0.70$ architectures. Average electric field and electric displacement field versus compressive strain ϵ in c,d) square and e,f) hexagonal architectures.

representing current void and matrix subdomain configurations, $\Omega = \Omega_v + \Omega_m$. The applied electric field has a constant magnitude; therefore, $\bar{E}_2 = E_{app}$. Thus, the electric field can be expressed as

$$\bar{E}_2 = \bar{E}_{2,v} + \bar{E}_{2,m} \quad (1)$$

where $\bar{E}_{2,v}$ and $\bar{E}_{2,m}$ are the average electric field magnitudes in the void and matrix subdomains, respectively. Consequently, the electric displacement magnitude and the effective permittivity can be expressed as

$$\bar{D}_2 = \epsilon_0 (\epsilon_v \bar{E}_{2,v} + \epsilon_m \bar{E}_{2,m}) \quad (2)$$

$$\epsilon_2^* = (\epsilon_v \bar{E}_{2,v} + \epsilon_m \bar{E}_{2,m}) / E_{app} \quad (3)$$

respectively. Equation (3) shows the dependence of effective permittivity on the field distribution in the void and matrix subdomains. When the electric field is more heavily distributed in the matrix subdomain, the DE architecture will exhibit a higher effective permittivity; conversely, an architecture with more field distributed in the void subdomains will exhibit a lower effective permittivity.

Figure 2c,d shows the change in the normalized electric field, \bar{E}_2/E_{app} , and electric displacement field, $\bar{D}_2/(\epsilon_0 E_{app})$, for the square architecture (with a demonstrative $c_v = 0.50$) under compression. The average electric field in the matrix subdomain, $\bar{E}_{2,m}$, increases with applied strain. Moreover, $\bar{E}_{2,m}$ increases at a faster rate after the onset of instability; and

the average electric field in the void subdomains monotonically decreases by the same amount. The total average electric field, $\bar{E}_{2,v} + \bar{E}_{2,m} = E_{app}$, does not change with deformation. The electric displacement variations in the void and matrix subdomains follow a similar trend. Since the polyurethane matrix has a higher relative permittivity, the total electric displacement field in the square unit cell increases with compression (Figure 2d). Figure 2e,f shows the corresponding results for the hexagonal architecture with $c_v = 0.70$. As in the square architecture, $\bar{E}_{2,m}$ increases with applied strain in the hexagonal architecture beyond the critical strain. Prior to instability, however, the average electric field in the hexagonal architecture decreases with compression. Consequently, the total electric displacement field in the hexagonal architecture decreases prior to instability and then proceeds to increase.

The variations in field distribution stem from the increase in matrix volume fraction as well as micro-structural transformation during deformation. In both architectures, c_m monotonically increases with compression and the rate of increase is significantly higher after the onset of instability (Figure S4, Supporting Information). Therefore, in the post-buckling regime ($\epsilon > \epsilon_{cr}$), the influence of increasing c_m dominates and both architectures exhibit an increase in $\bar{E}_{2,m}$ with ϵ . In the pre-buckling regime ($\epsilon < \epsilon_{cr}$), both architectures have a lower rate of increase in c_m . Before buckling, the circular voids gradually transform into ellipses under compression—major axis perpendicular to the applied field; hence, the electric field “passing” through the voids effectively increases.

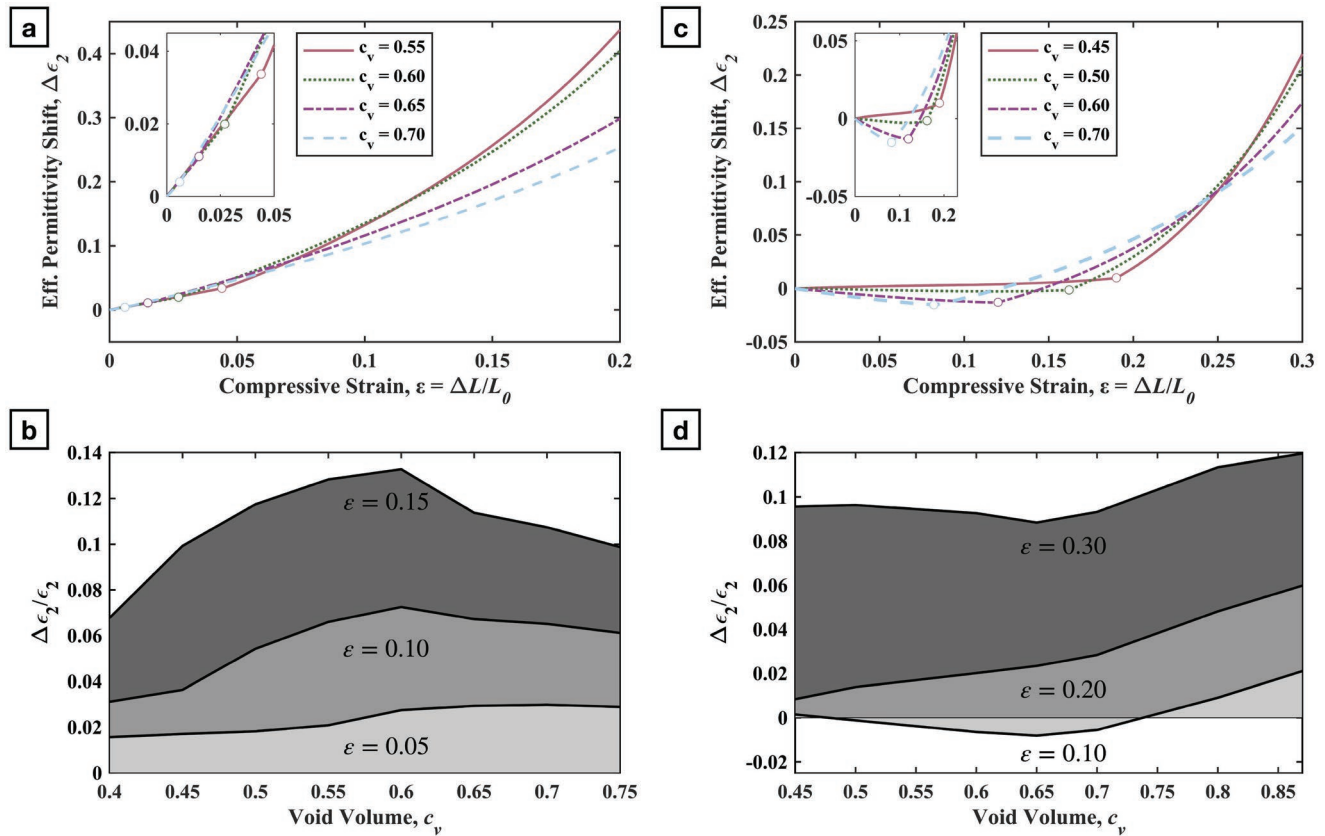


Figure 3. Numerical simulation of effective permittivity shift, $\Delta\epsilon_2$, in unit cells with varying void volume, c_v , and of parametric sweep for design tunability with varying c_v . a, b) Numerical simulation results for square unit cells. c, d) Numerical simulation results for hexagonal unit cells.

To quantify the corresponding decrease in the matrix electric field distribution, we analyzed the electrical response of both architectures with elliptical voids of constant $c_v = 0.7$ in the absence of deformation (the geometries are shown in Figure S6a,b, Supporting Information). Figure S6c shows the relative change in average electric field in the matrix subdomain, $\Delta\bar{E}_{2,m}/\bar{E}_{2,m}^*$, as a function of aspect ratio, r_1/r_2 . Here, $\Delta\bar{E}_{2,m} = \bar{E}_{2,m} - \bar{E}_{2,m}^*$ where $\bar{E}_{2,m}^*$ is the average electric field when $r_1/r_2 = 1$. The $\bar{E}_{2,m}$ decreases in both architectures with an increase in aspect ratio. However, in the hexagonal architecture $\bar{E}_{2,m}$ decreases more than its square counterpart. In the pre-buckling regime, void shape transformation plays a more dominant role in the hexagonal architecture, while matrix volume fraction primarily dictates the behavior in the square architecture. In summary, void shape transformation and increasing volume fraction exhibit opposing effects on the matrix electric field distribution, highlighting an important pair of mechanisms to exploit through geometric design.

Figure 3 shows the induced shift in effective permittivity, $\Delta\epsilon_2 = \epsilon_2^* - \epsilon_2$, versus compressive strain ϵ , for square and hexagonal architectures; ϵ_2^* and ϵ_2 denote the effective permittivity in the deformed configuration and in the undeformed state, respectively. Figure S5, Supporting Information, illustrates the dependence of ϵ_2 on the initial void volume fraction in both architectures. The effective permittivity in the square architecture increases monotonically with compression; notably, ϵ_2^* increases more rapidly beyond the onset of instability due

to the significant reduction in the void volume fraction. This numerical study indicates that the square architectures exhibit this behavior for initial void volume fractions $c_v = 0.40 - 0.75$ (Figure 3a). In contrast, the effective permittivity in the hexagonal architectures does not always increase with applied strain. The effective permittivity in hexagonal architectures with void volume fractions $c_v \lesssim 0.47$ monotonically increases with applied strain (Figure 3c). However, hexagonal architectures with void volume $c_v \gtrsim 0.47$ exhibit a negative deformation-induced permittivity shift before the onset of instability. Beyond this critical strain, the permittivity increases with the compressive strain.

The normalized permittivity shift, $\Delta\epsilon_2/\epsilon_2$ indicates the tunability of effective permittivity during applied strain. Figure 3b,d displays $\Delta\epsilon_2/\epsilon_2$ as a function of void volume fraction at different levels of applied strain in the square and hexagonal architectures; the void packing limits for the square and hexagonal architectures are $c_{v,th} = 0.785$ and $c_{v,th} = 0.907$, respectively. In the square architectures, the maximum tunability at small strain levels is achieved with higher void volume fractions (Figure 3b). However, at strains $\epsilon > \epsilon_{cr}$, the maximum permittivity shift in the square architectures is observed when $c_v = 0.60$ (Figure 3b). At compressive strain $\epsilon = 0.30$, hexagonal architectures with $c_v = 0.65$ exhibit the lowest normalized effective permittivity shift (Figure 3d). However, $\Delta\epsilon_2/\epsilon_2$ increases in hexagonal architectures with $c_v > 0.65$ (Figure 3d).

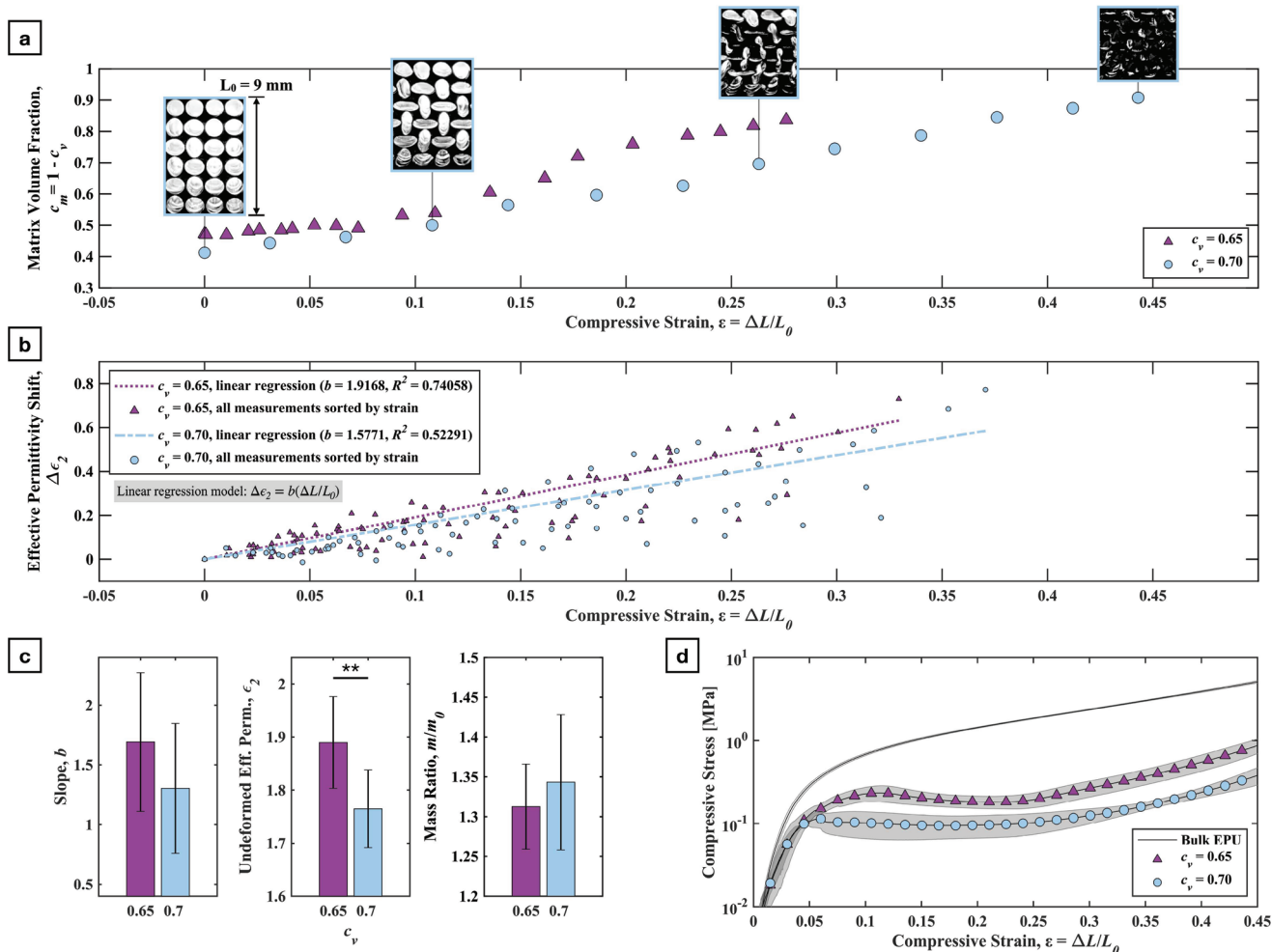


Figure 4. Experimental characterization of effective permittivity shift and mechanical properties of square architectures under finite strain with theoretical void volumes $c_v = 0.65$ and 0.70 . a) Change in matrix volume fraction under finite compression. b) Raw measurements and linear regression of shift in effective permittivity in architectures under finite compression. c) Between-sample comparison of effective permittivity shift linear regression slope, undeformed effective permittivity (statistically significant difference with $p = 0.0056$), and ratio of experimental and theoretical mass for all characterized samples ($m_0 = 4.25$ and 3.65 g for $c_v = 0.65$ ($N = 9$) and 0.70 ($N = 8$), respectively). d) Compressive behavior of bulk elastomeric polyurethane material, architecture with $c_v = 0.65$ ($N = 8$), and architecture with $c_v = 0.70$ ($N = 8$).

4. Experimental Characterization of Electromechanical Response

We tested the square and hexagonal architectures under compression to experimentally characterize their electromechanical coupling behavior. During this process, we determined the mechanical and dielectric properties of the architectures.

4.1. Square Architecture

Figure 4a illustrates the mechanical buckling that occurs in the square architectures under compression as well as the corresponding shift in their cross sectional matrix area, A_m (additional images of square architecture buckling with $c_v = 0.65$, 0.70 in Figure S7, Supporting Information). The matrix area A_m provides a direct estimate for the matrix volume fraction, $c_m \approx A_m$. During this primarily homogeneous buckling pattern,

the circular channels deform into a periodic pattern of horizontal and vertical elliptical channels leading to an increase in c_m ; the matrix volume fraction increases in a linear fashion as the architecture deforms.^[29,44] However, the initial matrix volumes in the experimental specimens were higher than their theoretical values. We observed a difference in matrix volume ($c_{m,exp} - c_m$) $c_m^{-1} \approx 0.23$ and 0.30 for $c_m = 0.35$ and 0.30 , respectively, in the demonstrative samples depicted in Figure 4a. This discrepancy is due to the dimensional accuracy of the fabrication method. While within the reported accuracy for the elastomeric polyurethane, the wall thicknesses were at least $40 \mu\text{m}$ larger than designed.

We characterized the permittivity shift, $\Delta\epsilon_2$, in square architecture specimens with either $c_v = 0.65$ or $c_v = 0.70$ volume fractions under finite compressive strain $\epsilon = \Delta L/L_0$ (L and L_0 are the thicknesses of the specimens under compression and in their undeformed states, respectively). For each sample set with a given c_v , we sorted all $\Delta\epsilon_2$ measurements by ϵ and

described the sorted values with a linear regression, $\Delta\epsilon_2 = b\epsilon$ (illustrated with R^2 values in Figure 4b). These linear models indicate $\Delta\epsilon_2 = 0.38$ and 0.31 at $\epsilon = 0.20$ in square architectures with $c_v = 0.65$ and 0.70 , respectively. Although slightly higher, these demonstrative models agree well with the shift predicted computationally (numerical $\Delta\epsilon_2 = 0.29$ and 0.25 for $c_v = 0.65$ and 0.70 , respectively; Figure 3a). In both the numerical and experimental studies, the shift in effective permittivity in the compressed square architecture relies on its relative increase in matrix volume fraction rather than the electric field distribution across its constituents. The sudden increase in effective permittivity observed computationally upon reaching critical strain is within the measurement tolerance of the experimental study.

We performed the same linear regression on each specimen's $\Delta\epsilon_2$ to gain insight into their measurement and fabrication consistency. On average, the square architectures with $c_v = 0.65$ increase in ϵ_2^* more rapidly under compressive strain and exhibit a significantly larger ϵ_2 in their undeformed state (Figure 4c). However, we observed variation within samples grouped by c_v likely due to inconsistencies in manufacturing quality. While dimensional accuracy during printing should remain the same within sample groups, residual liquid prepolymer can remain in the void channels prior to their final thermal cure if not thoroughly cleaned out. The experimental and theoretical mass ratio of the specimens, m/m_0 , provides an estimate of the residual resin in their void channels ($m_0 = 4.25$ and 3.65 g for $c_v = 0.65$ and 0.70 , respectively; Figure 4c). The spread of the mass ratio within each sample group illustrates the variation in residual resin that remained in the specimens after manufacturing and, ultimately, that led to variability of effective permittivity shift under deformation within each sample group.

Regardless of this residual mass, there is a clear difference in the compressive behavior between sample groups compared to that of the bulk elastomeric polyurethane (Figure 4d). The square architectures exhibit a similar compressive modulus, regardless of c_v , that is lower than that of the bulk elastomeric polyurethane ($E_{\text{comp}} \approx 1.92$ MPa and 7.11 MPa at $\epsilon = 0.02$, respectively). The compressive behavior of the square architectures diverges before reaching their critical buckling stress; more porous architectures exhibit a lower critical stress than their denser counterparts (yield stress $E_y = 0.23$ MPa at $\epsilon = 0.11$ and $E_y = 0.11$ MPa at $\epsilon = 0.05$ for architectures with $c_v = 0.65$ and 0.70 , respectively).

4.2. Hexagonal Architecture

Figure 5 summarizes the experimental characterization of the hexagonal architecture. Figure 5a illustrates the mechanical instability that occurs in the hexagonal architectures as they are compressed (additional images of hexagonal architectures buckling with $c_v = 0.60, 0.70$ in Figure S8, Supporting Information). The overall buckling pattern agrees with numerical simulations; the circular channels deform into rows of diagonally-oriented elliptical channels.^[16] As in the case of the square architecture, the matrix volume fraction increases linearly under compression. The hexagonal samples exhibit a larger discrepancy in initial matrix volumes c_m compared to theoretical values. We observed a difference in matrix volume $(c_{m,\text{exp}} - c_m)c_m^{-1} \approx 0.37$

and 0.55 for $c_m = 0.40$ and 0.30 , respectively, in the demonstrative samples depicted in Figure 5a. Notably, the mechanical collapse of the hexagonal architecture occurs in a more sequential manner—buckling begins at the bottom fixed surface and proceeds in a row-by-row fashion (experimental setup in Figure S9, Supporting Information). This layer-by-layer collapse is common among elastomeric structures with periodic architectures.^[45–50] While the presence and orientation of localized deformation bands is highly dependent on strain rate and loading conditions, Wagner et al., controlled the activation of local deformation bands by designing lattices with bend- or stretch-dominated topology.^[45,49]

The hexagonal architectures exhibit shifts of $\Delta\epsilon_2 = 0.50$ and 0.34 at $\epsilon = 0.25$ with $c_v = 0.60$ and 0.70 , respectively (Figure 5b). Within the samples grouped by c_v , the hexagonal architectures with $c_v = 0.60$ demonstrate a more rapid shift $\Delta\epsilon_2$ than their counterparts with $c_v = 0.70$ during compression (Figure 5c). However, the two sample groups did not exhibit a significant difference in effective permittivity ϵ_2 in their undeformed state. The samples with $c_v = 0.70$ contained more residual resin and exhibited a relatively large variability in residual mass—leading to an inflated and inconsistent effective permittivity (Figure 5c). The experimental permittivity tuning results differ from the computational predictions in two distinct ways. First, an initial decrease in permittivity at small applied strains is not observed experimentally. Second, the experimental permittivity shifts at high strains are larger than the computational predictions. For example, specimens with volume fraction $c_v = 0.70$ exhibit an experimental increase in permittivity of $\Delta\epsilon_2 = 0.34$ at an applied strain of $\epsilon = 0.25$; the predicted increase in permittivity is only $\Delta\epsilon_2 = 0.09$.

One contributing factor in these differences is the variability and positive bias in matrix mass due to excess infill. As seen in Figure 3d, there is a narrow range of void volume fractions ($c_v = 0.5 - 0.75$) that exhibit a decrease in permittivity at small strains. The excess infill may have pushed the experiment results out of this regime. Additionally, the experimental variability in specimen fabrication and the tolerance of the dielectric measurement may have limited our ability to resolve this predicted decrease in effective permittivity. We also speculate that the field distributions predicted in the computational model are more sensitive to the spatial inhomogeneities observed in the experiment than the matrix densification. Due to these factors, we believe that the matrix collapse is the dominant permittivity tuning mechanism observed experimentally in the hexagonal architectures.

The hexagonal architecture, regardless of c_v , exhibits a similar compressive modulus to that of the square architecture ($E_{\text{comp}} \approx 1.90$ MPa and 1.92 MPa, respectively, at $\epsilon = 0.02$; Figure 5d). However, the hexagonal architectures reach a higher critical stress before buckling instability occurs; the architectures with $c_v = 0.60$ yield under $E_y = 0.38$ MPa at $\epsilon = 0.18$ while those with $c_v = 0.70$ yield $E_y = 0.20$ MPa at $\epsilon = 0.13$ (Figure 5d). The humps shown in the stress response of the hexagonal architectures are consistent with the row-by-row collapse of the unit cells.^[45] In both unit cell designs, the architectures with a lower void volume may require less compressive strain for increases in ϵ_2 , but more porous architectures still exhibit a considerable shift in effective permittivity and deform more easily as a flexible substrate for electronics.

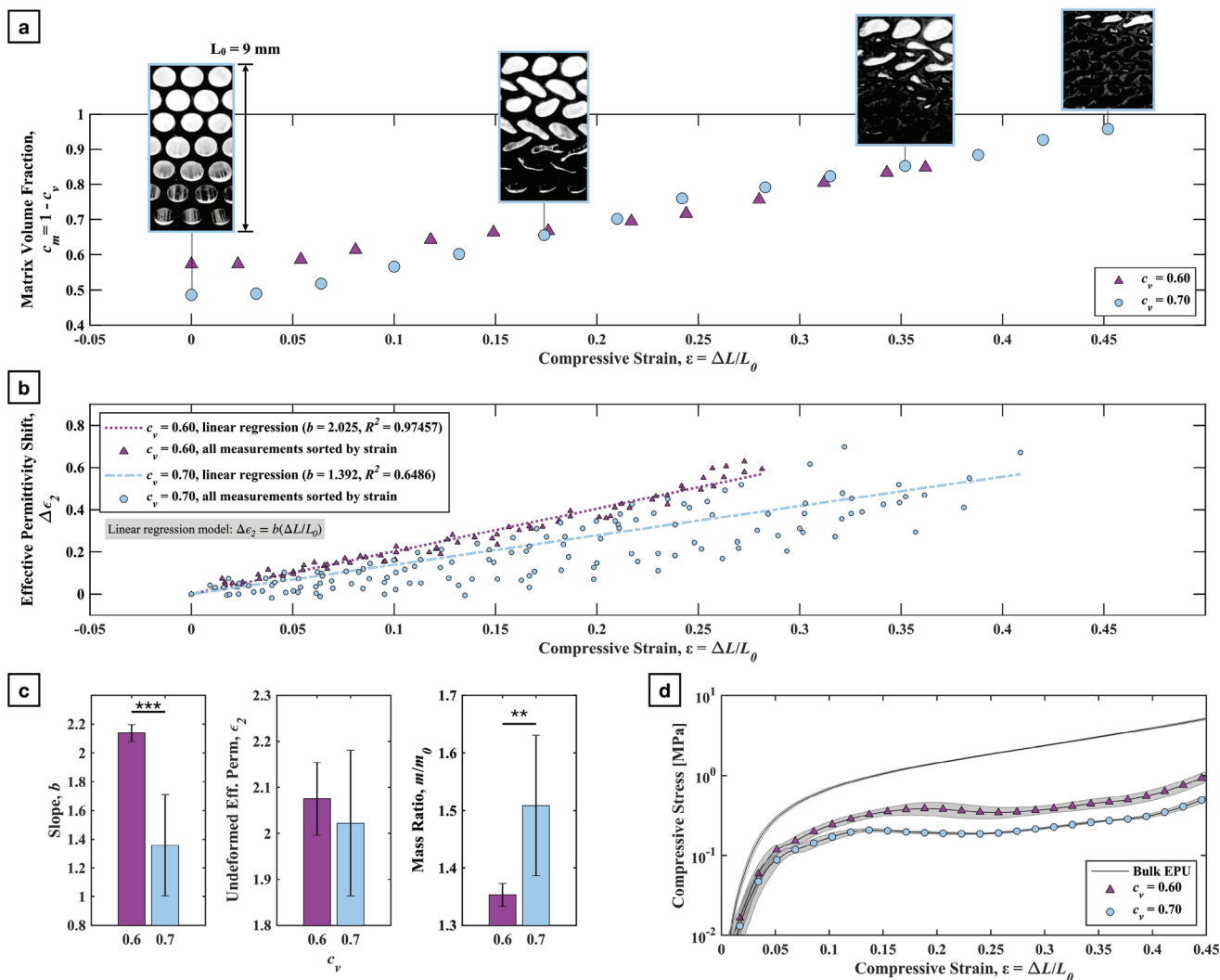


Figure 5. Experimental characterization of effective permittivity shift and mechanical properties of hexagonal architectures under finite strain with theoretical void volumes $c_v = 0.60$ and 0.70 . a) Change in matrix volume fraction under finite compression. b) Raw measurements and linear regression of shift in effective permittivity in architectures with under finite compression. c) Between-sample comparison of effective permittivity shift linear regression slope (statistically significant difference with $p = 0.00013$), undeformed effective permittivity, and ratio of experimental and theoretical mass for all characterized samples ($m_0 = 5.58 \text{ g}$ and 4.19 g for $c_v = 0.60$ ($N = 7$) and 0.70 ($N = 9$), respectively; statistically significant difference between groups with $p = 0.0049$). d) Compressive behavior of bulk elastomeric polyurethane material, architecture with $c_v = 0.60$ ($N = 8$), and architecture with $c_v = 0.70$ ($N = 8$).

5. Strain-Tuning of Microstrip Antenna Resonance Frequency

Controlling the effective permittivity of a dielectric substrate by mechanical deformation offers a novel strategy for tuning the performance of flexible RF devices. To illustrate the potential of this strain-tuning mechanism, we demonstrated the application of the DE architecture as a substrate for an aperture coupled microstrip patch antenna.^[51] The aperture-coupled feed structure mitigates the impact of moving or flexible feed lines in the measurement setup and accommodates testing multiple antenna substrate samples (assembly schematic in Figure 6a). The antenna design operates within the mobile communication frequency range ($f = 500 \text{ MHz}$ to 3 GHz) through the entire compression of the architected substrate. We fabricated and

characterized two architected dielectric elastomer substrates; they consisted of hexagonal unit cells with $c_v = 0.60$ or 0.70 (see Supporting Information for full details of the antenna design, layout, and 3D printed substrate.)

Figure 6c shows the measured antenna reflection coefficient, S_{11} , over the prescribed frequency range, $f = 1\text{--}2 \text{ GHz}$, as the substrate is compressed. In this design, the two predominant tuning mechanisms are a shift in antenna resonance frequency, f_r , caused by a change in substrate ϵ_r ; and a change in operating bandwidth which is influenced, in part, by changes in substrate thickness, L . For this design, an increased permittivity results in a lower resonance frequency. In both substrates, $c_v = 0.60$ and 0.70 , the shift in effective permittivity of the dielectric architecture causes a corresponding shift in the resonance frequency, f_r , of the patch antenna (Figure 6d). The antenna

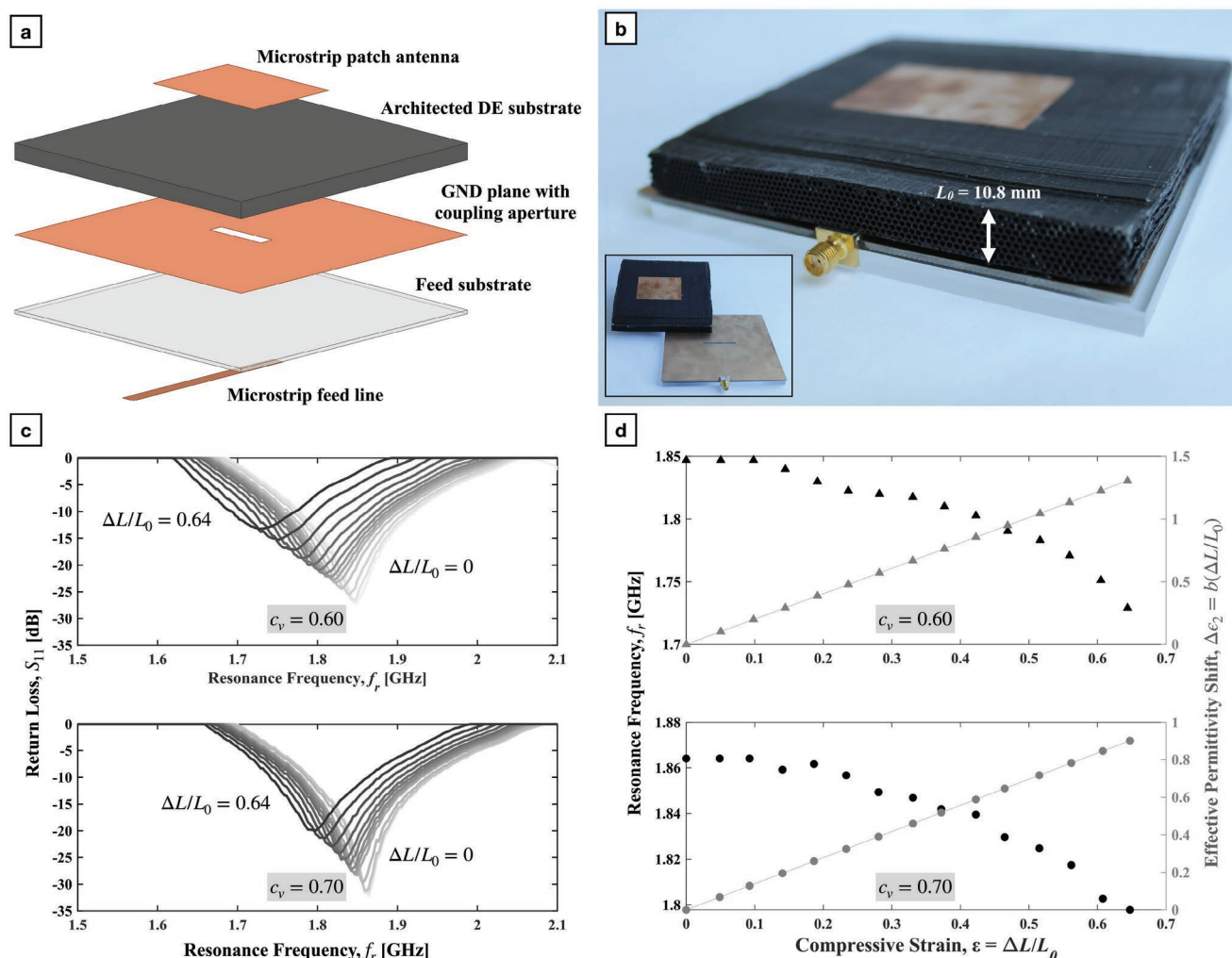


Figure 6. Demonstration of microstrip patch antenna with architected dielectric elastomer substrate. a) Exploded view of antenna assembly. b) Fabricated microstrip patch antenna with architected hexagonal dielectric elastomer substrate ($L_0 = 10.8$ mm). c) Measured return loss, S_{11} , curves for void volumes $c_v = 0.60$ and 0.70 . d) Experimental characterization of resonance frequency, f_r , with linear regression of shift in effective permittivity $\Delta\epsilon_2 = b(\Delta L/L_0)$ under compressive strain $\epsilon = \Delta L/L_0$ for void volumes $c_v = 0.60$ and 0.70 (markers placed on linear regression as visual aid).

assembly was compressed to a strain of $\epsilon \approx 0.65$ and its reflection coefficients were measured across the frequency range. The hexagonal substrate with $c_v = 0.60$ exhibits a larger shift in resonance frequency $|\Delta f_r| = 117$ MHz during compression than the sample with larger void volume $c_v = 0.70$ ($|\Delta f_r| = 66$ MHz).

The shift in resonance frequency within the UHF-band demonstrates the applicability of a compressive permittivity-tunable substrate for frequency agility applications. This can be applied in sensing and communication applications where a small but significant shift in frequency can be produced by a precise deformation state. Additionally, through additive manufacturing these systems are not limited to a single architecture arrangement within a device. The varied architectures can elicit diverse responses across a device based on electrical needs; for example, grading dielectric regions for feed structures versus radiating elements. This adds a novel design dimension to exploit that would enable devices with additional capabilities rooted in electromechanical responses, rather than in electrical circuit element design alone.

6. Conclusion

In summary, we characterized, with numerical simulations and experimental measurements, the electromechanical response of two dielectric elastomer architectures. The distinct buckling patterns in the square and hexagonal architectures and subsequent matrix densification result in a shift in their effective permittivity. We demonstrated that the porosity of the periodic structures provides a tuning mechanism for the onset of a mechanical instability in the elastomer. The additive fabrication route selected for these architectures allows rapid customization of their unit cell geometry and, as a result, their corresponding electromechanical response. We observed effective permittivity shifts $\Delta\epsilon_2 > 0.7$ under compressive strains $\epsilon < 0.35$. The square and hexagonal architectures are more flexible than their bulk polyurethane counterpart—beneficial for flexible electronic devices; their effective mechanical behavior, such as compressive modulus and critical buckling stress, is easily tuned with porosity. We demonstrated that the 3D printed

architectures function as a soft, flexible substrate for a microstrip patch antenna and exhibit a tunable shift in resonance frequency during deformation, $|\Delta f_r| > 110$ MHz, for hexagonal architectures with $c_v = 0.60$.

Although the DLP fabrication method selected for this study boasts high resolution and fast printing speeds, the void channels proved difficult to consistently clear of liquid pre-polymer with the current solvent, isopropyl alcohol. To address variation in dielectric properties and physical response to deformation between samples, we can explore the solubility of the polyurethane pre-polymer in more aggressive solvents such as propylene glycol or isopropylacetone. Looking forward, the selection of 3D printing as the fabrication method is particularly useful for grading porosity; this strategy could be used to constrain the deformation of a soft sensing array in certain directions or to locally tune its effective stiffness.^[25,52,53] Regardless of manufacturing quality, local deformation bands appeared consistently in the hexagonal architecture under compression. We will continue to investigate the mechanics leading to this phenomenon and its implications on the electromechanical response of the system. Although we focused on a single material system for the dielectric architecture, Goshkoderia et al. numerically demonstrated the potential of incorporating high permittivity, stiff inclusions in these architectures, either randomly or in a periodic fashion.^[29] The inclusions effectively act as an array of micro-capacitors; varying their shape and periodicity provides further customization of the dielectric response in the architectures.^[29]

The microstrip patch antenna demonstrated here could be expanded to that of an array. A soft, conformable antenna array of this nature could allow shape detection or the characterization of spatially varying compression. Dielectric elastomer architectures experimentally show promise for a variety of application spaces; elastomeric composites can facilitate regulation of effective dielectric properties in the optical and millimeter wave regimes via small mechanical deformations. Physically reconfigurable metamaterials offer adaptive resonance properties in electromagnetic, acoustic, and optical fields. These strain-tunable dielectric materials lend themselves to flexible hybrid electronics and will advance the research landscape of adaptive communication devices.

7. Statistical Analysis

The effective permittivity shifts in Figures 4b and 5b are linear regressions of all $\Delta\epsilon_2$ measurements sorted by ϵ for each sample set of square and hexagonal architectures. The legends in Figures 4b and 5b list the slope and R^2 values for each linear regression. We also performed a linear regression on the shift in $\Delta\epsilon_2$ for each specimen. Figures 4c and 5c contain the average and standard deviation of the linear regression slope for each sample set of square and hexagonal architectures; the following number of samples were characterized: $N = 9$ square samples with $c_v = 0.65$, $N = 8$ square samples with $c_v = 0.70$, $N = 7$ hexagonal samples with $c_v = 0.60$, and $N = 9$ hexagonal samples with $c_v = 0.70$. Figures 4c and 5c also contain the average and standard deviation of the undeformed effective permittivity ϵ_2 and the mass ratio m/m_0 for each sample set of square and hexagonal architectures.

For each of the comparisons between c_v groups in Figures 4c and 5c, we conducted a two-sample t -test. The resulting p -values for each comparison are listed in Figures 4c and 5c and their level of statistical significance is illustrated with corresponding asterisks; ** represents a p -value less than 0.01 and *** represents a p -value less than 0.001.

The compressive behavior in Figures 4d and 5d is the average and standard deviation (shaded area) of each sample set with the following sample set sizes: bulk EPU ($N = 7$), square architectures $c_v = 0.65$ and 0.70 ($N = 8$), hexagonal architectures $c_v = 0.60$ and 0.70 ($N = 8$).

8. Experimental Section

This section includes the experimental details of architecture fabrication, effective permittivity measurement, mechanical characterization, and measurement of microstrip patch antenna response.

Fabrication of Experimental Architectures: The elastomeric polyurethane resin was a proprietary formulation (EPU 40, Carbon 3D, Inc.) 3D printed on a Carbon 3D M1 printer. Following the layer-by-layer photocure, the polyurethane pieces were cleaned of uncured liquid resin with isopropyl alcohol and, subsequently, placed in a thermal oven for 8 h at 120 °C. Figure S2, Supporting Information, displays a completed print of the polyurethane architectures, these specimens were used for characterizing the shift in effective permittivity during compression and Figure S10, Supporting Information, displays a completed print of the architectures used for the microstrip antenna demonstration.

Buckling Demonstration: To experimentally characterize the matrix volume in the square and hexagonal architectures under compressive strain, photographs were taken of the samples and, using ImageJ software, converted into binary images for a black and white pixel count. For each image in the compression sequence, the black pixel counts were divided by the total pixel count to calculate the current matrix volume. The thickness of the samples, L , during compression was measured from the same images with ImageJ software and used to calculate the compressive strain, $\epsilon = \Delta L/L_0$ (L_0 is the thickness of the samples in their undeformed state).

Effective Permittivity Characterization: To experimentally measure $\Delta\epsilon_2$, a parallel plate capacitor model consisting of a dielectric disk with diameter D placed between two circular electrodes of the same diameter was assumed. A custom fixture allowed to compress the samples between two electrode plates (Figure S11, Supporting Information). An edge correction in the capacitance measurements (illustrated in Figure S11, Supporting Information) was also included. The experimental ϵ_2^* of a compressed sample with thickness L (m) is defined as:

$$\epsilon_2^* = \frac{C - C_e(L)}{C_n(L)} \quad (4)$$

where C (F) is the measured capacitance; $C_e(L)$ (F) is the edge capacitance due to the fringing field at the edge of the electrodes; and $C_n(L) = \epsilon_0 A L^{-1}$ (F) describes the normal capacitance through air as if the electric field were uniformly distributed and normal to the inner surfaces of the electrodes ($\epsilon_0 = 8.85 \times 10^{-12}$ F m⁻¹ is vacuum permittivity; $A = 0.0012$ m² is the electrode area).^[54] The effective permittivity of the architectures in their undeformed state, ϵ_2 , is $\epsilon_2 = \epsilon_2^* | L_0$.

Prior to characterizing the shift in effective permittivity of any samples, the characteristic edge capacitance function $C_e(L)$ of the experimental fixture was obtained to account for any differences in the physical surroundings of the experimental fixture. The same characteristic function $C_e(L)$ was used to calculate the effective permittivity for all samples. At thicknesses L (m) between the electrode plates, the edge capacitance is defined as

$$C_e(L) = C_d - C_n(L) \quad (5)$$

where C_L (F) is the measured capacitance with only air between the plates and $C_n(d) = \epsilon_0 A d^{-1}$ (F) is the normal capacitance through air as if the electric field were uniformly distributed and normal to the inner surfaces of the electrodes.^[54] The capacitance values, C_L , at each thickness, L , in Equation (5) were calculated from the corresponding impedance between the electrodes, measured by an HP 4194A Impedance Analyzer, as follows

$$C_L = \frac{1}{2\pi f |Z| \sin \phi} \quad (6)$$

where $f = 1$ MHz is the measurement frequency, $|Z|$ (Ω) is the impedance magnitude, and ϕ (rad) is the impedance phase. This measurement frequency, $f = 1$ MHz, was selected based on the feature size within the porous architectures. The signal wavelength at this frequency was significantly large compared to the pore sizes ($\lambda_{3\text{GHz}} \approx 10$ cm, pore size ≈ 1 mm). The capacitance values of the samples, C (F), at each compressive thickness in Equation (4) were collected in the same way. The compressive strain, $\epsilon = \Delta L/L_0$, was measured from photographs of the samples taken at each compression step. The initial thickness of the samples, L_0 , and their thickness during compression, L , were measured from these images with ImageJ software and used to calculate ϵ .

As validation of this characterization method, the effective permittivity of solid elastomeric polyurethane disks with varying thickness on each day of measurement were also measured following the same procedure. These measurements are illustrated in Figure S13, Supporting Information. These measurements show good agreement with the reported relative permittivity, $\epsilon_m = 4$.^[40] The relative permittivity of the bulk elastomeric polyurethane ($\epsilon_m = 4$) was characterized per the standard ASTM D150 by Carbon3D, Inc.^[43]

Mechanical Testing: The tensile behavior of the bulk elastomeric polyurethane material was performed according to the International Organization for Standardization (ISO) 37 method with a type four dumbbell sample geometry ($N = 11$). The test was performed at 200 mm min⁻¹ on a Z010 Zwick Roell machine with a 10 kN load cell and pneumatic grips pressurized to 85 psi. The compressive behavior of the bulk elastomeric polyurethane material was characterized using a cylindrical sample geometry with diameter $D = 29$ mm and thickness $L_0 = 12.5$ mm. The samples ($N = 7$) were compressed at a rate of 12 mm min⁻¹ on a Z010 Zwick Roell machine with a 10 kN load cell.

The compressive behavior of the unit cell geometries was characterized using a cylindrical sample geometry with diameter $D = 12$ mm. The thickness of the samples depended on the unit cell; the samples with a square unit cell geometry ($c_v = 0.65$ or 0.70 , $N = 8$ sample of each) were cylinders with thickness $L_0 = 6.64 \pm 0.068$ mm and the samples with a hexagonal unit cell geometry ($c_v = 0.60$ or 0.70 , $N = 8$ samples of each) were cylinders with thickness $L_0 = 5.83 \pm 0.051$ mm. The samples were compressed at a rate of 0.01 mm s⁻¹ on a Z010 Zwick Roell machine with a 10 kN load cell.

Antenna Response Characterization: To characterize the shift in resonance frequency of the microstrip patch antenna, the assembly (Figure S14, Supporting Information) was compressed on a Z010 Zwick Roell machine with a 10 kN load cell. To prevent direct contact from the metal compression plate with the radiating element, Rohacell 51 HF (thickness $t = 2.5$ cm, relative permittivity $\epsilon_r = 1.057$, and loss tangent $\tan \delta < 0.0002$) was placed above and below the device. The compression was paused at $\Delta L = 0.5$ mm increments to collect the complex reflection coefficient from 1–2 GHz with a miniVNA Tiny Vector Network Analyzer. This frequency range was higher than the 1 MHz dielectric measurement frequency; however, the void architectures were sufficiently small compared to the operating wavelength so the structure was expected to exhibit a similar permittivity shift. The geometric scale of the architectures could be tuned to target specific frequency regimes. While a large substrate thickness, or an excess of unit cell rows, could contribute to loss and prevent signal penetration, the experimental device substrate thickness, $t = 10.8$ mm, was functionally sufficient. The Supporting Information includes a detailed description of the design and analysis of the antenna.

Supporting Information

Supporting Information is available from the Wiley Online Library or from the author.

Acknowledgements

The authors acknowledge the support of the Air Force Research Laboratory.

Conflict of Interest

The authors declare no conflict of interest.

Data Availability Statement

The data that support the findings of this study are available from the corresponding author upon reasonable request.

Keywords

flexible hybrid electronics, mechanical metamaterial, physical reconfiguration, strain programming

Received: February 24, 2022

Revised: July 7, 2022

Published online:

- [1] M. Choi, J. H. Choe, B. Kang, C. G. Choi, *Curr. Appl. Phys.* **2013**, *13*, 1723.
- [2] Z. H. Jiang, S. Yun, F. Toor, D. H. Werner, T. S. Mayer, *ACS Nano* **2011**, *5*, 4641.
- [3] J. P. Turpin, J. A. Bossard, K. L. Morgan, D. H. Werner, P. L. Werner, *Int. J. Antennas Propag.* **2014**, *2014*, 429837.
- [4] S. Walia, C. M. Shah, P. Gutruf, H. Nili, D. R. Chowdhury, W. Withayachumnankul, M. Bhaskaran, S. Sriram, *Appl. Phys. Rev.* **2015**, *2*, 011303.
- [5] M. Kadic, G. W. Milton, M. van Hecke, M. Wegener, *Nat. Rev. Phys.* **2019**, *1*, 198.
- [6] R. Yahiaoui, J. P. Guillet, F. de Miollis, P. Mounaix, *Opt. Lett.* **2013**, *38*, 4988.
- [7] J. Li, C. M. Shah, W. Withayachumnankul, B. S. Ung, A. Mitchell, S. Sriram, M. Bhaskaran, S. Chang, D. Abbott, *Appl. Phys. Lett.* **2013**, *102*, 121101.
- [8] A. S. Kaddour, S. V. Georgakopoulos, *Proc. 2020 IEEE Int. Symp. on Antennas and Propagation and North American Radio Science Meeting, IEEECONF, IEEE, Piscataway, NJ* **2020**, pp. 545–546.
- [9] D. Sessions, A. Cook, K. Fuchi, A. Gillman, G. Huff, P. Buskohl, *Sensors* **2019**, *19*, 4808.
- [10] Y. Cui, R. Bahr, S. Van Rijs, M. Tentzeris, *Int. J. Microwave Wireless Technol.* **2021**, *13*, 727.
- [11] I. M. Van Meerbeek, C. M. De Sa, R. F. Shepherd, *Sci. Rob.* **2018**, *3*, eaau2489.
- [12] P. A. Xu, A. K. Mishra, H. Bai, C. A. Aubin, L. Zullo, R. F. Shepherd, *Sci. Rob.* **2019**, *4*, eaaw6304.
- [13] Y. Zhang, Y. Huang, T. Zhang, H. Chang, P. Xiao, H. Chen, Z. Huang, Y. Chen, *Adv. Mater.* **2015**, *27*, 2049.
- [14] I. Brener, S. Liu, I. Staude, J. Valentine, C. L. Holloway, *Dielectric Metamaterials*, Elsevier, New York **2020**.

- [15] N. V. Gorshkov, V. G. Goffman, M. A. Vikulova, I. N. Burmistrov, A. V. Kovnev, A. V. Gorokhovskiy, *J. Compos. Mater.* **2018**, 52, 135.
- [16] J. Li, Y. Wang, W. Chen, Y. S. Wang, R. Bao, *J. Sound Vib.* **2019**, 459, 114848.
- [17] K. Bertoldi, V. Vitelli, J. Christensen, M. Van Hecke, *Nat. Rev. Mater.* **2017**, 2, 17066.
- [18] K. Bertoldi, P. M. Reis, S. Willshaw, T. Mullin, *Adv. Mater.* **2010**, 22, 361.
- [19] R. Lakes, *Science* **1987**, 238, 551.
- [20] Y. Prawoto, *Comput. Mater. Sci.* **2012**, 58, 140.
- [21] B. Florijn, C. Coulais, M. Van Hecke, *Phys. Rev. Lett.* **2014**, 113, 175503.
- [22] M. J. Mirzaali, R. Hedayati, P. Vena, L. Vergani, M. Strano, A. A. Zadpoor, *Appl. Phys. Lett.* **2017**, 111, 5.
- [23] A. Rafsanjani, A. Akbarzadeh, D. Pasini, *Adv. Mater.* **2015**, 27, 5931.
- [24] P. Jiao, A. H. Alavi, *Int. Mater. Rev.* **2021**, 66, 365.
- [25] M. J. Mirzaali, S. Janbaz, M. Strano, L. Vergani, A. A. Zadpoor, *Sci. Rep.* **2018**, 8, 965.
- [26] S. Babae, J. T. Overvelde, E. R. Chen, V. Tournat, K. Bertoldi, *Sci. Adv.* **2016**, 2, 2.
- [27] J. Li, V. Slesarenko, S. Rudykh, *Soft Matter* **2018**, 14, 6171.
- [28] J. Li, S. Rudykh, *Composites, Part B* **2019**, 172, 352.
- [29] A. Goshkoderia, N. Arora, V. Slesarenko, J. Li, V. Chen, A. Juhl, P. Buskohl, S. Rudykh, *Int. J. Mech. Sci.* **2020**, 186, 105880.
- [30] S. Alharbi, R. M. Shubair, A. Kiourti, *IET Conf. Publ.* **2018**, 2018, 7.
- [31] B. Mohamadzade, R. M. Hashmi, R. B. Simorangkir, R. Gharai, S. U. Rehman, Q. H. Abbasi, *Sensors (Switzerland)* **2019**, 19, 10.
- [32] J. Trajkovikj, J. F. Zurcher, A. K. Skrivervik, *IEEE Antennas Propag. Mag.* **2013**, 55, 287.
- [33] Q. H. Abbasi, M. U. Rehman, X. Yang, A. Alomainy, K. Qaraqe, E. Serpedin, *IEEE Antennas Wireless Propag. Lett.* **2013**, 12, 1606.
- [34] D.-H. Kim, J.-H. Ahn, W. M. Choi, H.-S. Kim, T.-H. Kim, J. Song, Y. Y. Huang, Z. Liu, C. Lu, J. A. Rogers, *Science* **2008**, 320, 507.
- [35] B. C. Mac Murray, X. An, S. S. Robinson, I. M. Van Meerbeek, K. W. O'Brien, H. Zhao, R. F. Shepherd, *Adv. Mater.* **2015**, 27, 6334.
- [36] J. Morita, Y. Ando, S. Komatsu, K. Matsumura, T. Okazaki, Y. Asano, M. Nakatani, H. Tanaka, *Polymers* **2021**, 13, 842.
- [37] I. M. Van Meerbeek, B. C. Mac Murray, J. W. Kim, S. S. Robinson, P. X. Zou, M. N. Silberstein, R. F. Shepherd, *Adv. Mater.* **2016**, 28, 2801.
- [38] Z. Larimore, S. Jensen, P. Parsons, B. Good, K. Smith, M. Mirotznik, *Addit. Manuf.* **2017**, 15, 48.
- [39] D. Goswami, S. Liu, A. Pal, L. G. Silva, R. V. Martinez, *Adv. Funct. Mater.* **2019**, 29, 1808713.
- [40] EPU 40 - Elastomeric Polyurethane Resin for Carbon 3D Printers, <https://www.carbon3d.com/materials/epu-40/> (accessed: December 2021).
- [41] J. R. Tumbleston, D. Shirvanyants, N. Ermoshkin, R. Januszewicz, A. R. Johnson, D. Kelly, K. Chen, R. Pinschmidt, J. P. Rolland, A. Ermoshkin, E. T. Samulski, J. M. DeSimone, *Science* **2015**, 347, 1349.
- [42] T. J. Wallin, J. Pikul, R. F. Shepherd, *Nat. Rev. Mater.* **2018**, 3, 84.
- [43] Carbon DLS Accuracy for Engineering Materials - Carbon, <https://www.carbon3d.com/resources/dls-101/carbon-dls-accuracy-for-engineering-materials/> (accessed: December 2021).
- [44] T. Mullin, S. Deschanel, K. Bertoldi, M. C. Boyce, *Phys. Rev. Lett.* **2007**, 99, 084301.
- [45] D. W. Abueidda, M. Bakir, R. K. Abu Al-Rub, J. S. Bergström, N. A. Sobh, I. Jasiuk, *Mater. Des.* **2017**, 122, 255.
- [46] K. Bertoldi, M. C. Boyce, S. Deschanel, S. M. Prange, T. Mullin, *J. Mech. Phys. Solids* **2008**, 56, 2642.
- [47] H. Qiu, Y. Li, T. Guo, S. Tang, Z. Xie, X. Guo, *Materials* **2021**, 14, 1.
- [48] J. Chung, A. M. Waas, *AIAA J.* **2002**, 40, 974.
- [49] M. A. Wagner, T. S. Lumpe, T. Chen, K. Shea, *Extreme Mech. Lett.* **2019**, 29, 100461.
- [50] S. D. Papka, S. Kyriakides, *Acta Mater.* **1998**, 46, 2765.
- [51] C. A. Balanis, *Antenna Theory: Analysis and Design*, Wiley-Interscience, Hoboken, NJ **2005**.
- [52] R. C. Rumpf, J. Pazos, C. R. Garcia, L. Ochoa, R. Wicker, *Prog. Electromagn. Res.* **2013**, 139, 13030507.
- [53] C. R. Garcia, J. Correa, D. Espalin, J. H. Barton, R. C. Rumpf, R. Wicker, V. Gonzalez, *Prog. Electromagn. Res. Lett.* **2012**, 34, 75.
- [54] A. Scott, H. Curtis, *J. Res. Natl. Bur. Stand.* **1939**, 22, 747.